Structure–Property Correlation in Fe-Al_2O_3 *In Situ* Nanocomposite Synthesized by High-Energy Ball Milling and Spark Plasma Sintering

V. UDHAYABANU, K.R. RAVI, and B.S. MURTY

In the present study, Fe-10 vol pct Al_2O_3 *in situ* nanocomposite has been derived by high-energy ball milling of Fe_2O_3-Fe-Al powder mixture followed by the consolidation using spark plasma sintering (SPS). The consolidated nanocomposite has bimodal-grained structure consisting of nanometer- and submicron-sized Fe grains along with nanometer-sized Al_2O_3, and Fe_3O_4 particles. The mechanical property analysis reveals that compressive yield strength of Fe-10 vol pct Al_2O_3 nanocomposite is 2100 MPa which is nearly two times higher than that of monolithic Fe processed by Mechanical Milling and SPS. The strengthening contributions obtained from matrix, grain size, and particles in the synthesized nanocomposite have been calculated theoretically, and are found to be matching well with the experimental strength levels.

DOI: 10.1007/s11661-016-3627-z

I. INTRODUCTION

NANOCOMPOSITES in which both the matrix and the reinforcement are nanocrystalline or the nano-reinforcement in microcrystalline matrix exhibit superior mechanical properties compared to their microcrystalline counterparts with similar volume fractions of reinforcement particles. *In situ* formation of the reinforcement particles by powder metallurgy route is reported to overcome the difficulty in dispersion and segregation problems of very fine, nanosized reinforcement particles normally encountered in casting route.[1] Moreover, the *in situ* reinforcement particles are thermodynamically stable and compatible with the matrix. Mechanical alloying (MA) is a popular technique to synthesize nanocrystalline, amorphous, and intermetallic powders.[2] In addition to this, the development of nanocomposites by activating the displacement reactions where the metal oxides are reduced by more reactive metals is also established as one of the applications of MA.[3]

Matteazzi and LeCaer[3] have studied mechanically driven reduction reactions of various metal oxides such as V_2O_3, Cr_2O_3, MnO_2, Fe_2O_3, CoO, NiO, CuO, ZnO, Nb_2O_5, MoO_3, WO_3, and SiO_2 by aluminum in the synthesis of metal-alumina nanocomposites. There has been extensive research works on the reactive milling of CuO-Al and NiO-Al systems in order to synthesize Cu-, Ni-, NiAl-, and Ni_3Al-based nanocomposites in which *in situ* Al_2O_3 is the reinforcement.[4–18] Improved mechanical and physical properties have been observed after the consolidation of these nanocomposite powders.[15–18] There has been considerable amount of work on Fe_2O_3/Fe_3O_4 reduction by Al in high-energy ball milling with the view of synthesizing Fe-, FeAl-, and Fe_3Al-based nanocomposites with Al_2O_3 reinforcement.[3,19–25] However, most of the studies involving Fe_2O_3/Fe_3O_4 reduction by Al in high-energy ball milling are limited to powder synthesis, except the works by Ishonishi *et al.*[23] and Ravi *et al.*[24]

Consolidation of mechanically milled metal/alloys/composite powders is one of the critical steps involved in the fabrication of bulk nanostructured/nanocomposite materials. Conventional consolidation techniques such as hot extrusion, hot pressing, hot isostatic pressing, etc. are usually carried out at high temperatures for long duration, which may invariably result in coarsening of the nanosized grains present in the milled powders. In order to overcome the aforementioned difficulty, a few rapid sintering processes[26] such as high-velocity oxy fuel (HVOF), cold spraying, and spark plasma sintering have been developed for consolidation of the mechanically milled powders. Among these techniques, SPS has the main advantages of low sintering temperature and short sintering time, and hence it has greater potential in retaining the nanostructure after sintering. Moreover, studies on SPS process suggest that it has the capability in producing bimodal-grained microstructure in metallic materials. This is confirmed in the case of Fe,[27] Fe-C,[28] Ti-6Al-4V,[29] Ni,[30] and 14 Cr ODS alloys.[31] Obtaining simultaneous improvement in tradeoff mechanical properties such as strength and ductility is one of the interesting facets of the bimodal-grained microstructure. With the aid of SPS process, Srinivasarao *et al.*[27] prepared a bulk bimodal-grained iron

V. UDHAYABANU, Assistant Professor, is with the Department of Metallurgical and Materials Engineering, Visvesvaraya National Institute of Technology, Nagpur 400010, India. K.R. RAVI, Associate Professor, is with PSG Institute of Advanced Studies, Coimbatore 641 004, India. Contact e-mail: krravi.psgias@gmail.com B.S. MURTY, Head of Department, is with the Department of Metallurgical and Materials Engineering, Indian Institute of Technology Madras, Chennai 600 036, India.

Manuscript submitted April 19, 2015.
Article published online July 12, 2016

which has shown combination of extremely high fracture strength of 2249 MPa and a true strain of 40 pct. These results have substantiated the abovementioned comment on mechanical properties of the bimodal-grained microstructure. Interestingly, the authors' previous work on the spark plasma sintering of Fe_2O_3-Al-Fe powder mixture has also shown the formation of Fe-10 vol pct Al_2O_3 composites with bimodal-grained microstructure.[24] However, no systematic studies were carried out to understand the role of bimodal-grained structure on the mechanical behavior of spark plasma sintered Fe-10 vol pct Al_2O_3 composites.[24] To prevail over this inadequacy, present work has aimed to elucidate the role of bimodal-grained microstructure on the mechanical behavior of SPS consolidated Fe-10 vol pct Al_2O_3 composites. The strengthening mechanisms in the SPS-consolidated Fe-10 vol pct Al_2O_3 nanocomposite also have been investigated and discussed in detail.

II. EXPERIMENTAL DETAILS

High-energy milling was carried out in a planetary ball mill (Fritsch pulverisette-5) for Fe_2O_3-2.6 wt pct Al-89.6 wt pct Fe powder mixture in order to synthesize Fe-10 vol pct Al_2O_3 nanocomposite powder. Milling was carried out in the ball-to-powder ratio of 10:1 using tungsten carbide vials and tungsten carbide balls of 10-mm diameter. Toluene was used as process controlling agent to avoid oxidation and excessive cold welding of powders to vials and balls. The milling speed was maintained as 300 rpm. Milled powders were collected in every 5-hour interval for phase analysis. Phase and structural evolutions during milling and heating were analyzed using Shimadzu, XD-D1 diffractometer using Fe-K_α radiation. XRD scans were made with the step size of 0.02 deg and scan speed of 2 deg/min. Crystallite size calculation was made using Voigt X-ray peak profile analysis after eliminating the strain and instrumental broadening contributions.[32] The as-milled powders were consolidated by means of an SPS-1050 machine (Sumitomo Coal Mining, Japan) at 973 K (700 °C) and 1073 K (800 °C) for 5 minutes. The sintering temperatures were chosen based on previous studies on SPS consolidation of the ball-milled Fe[27] and Fe-10 vol pct Al_2O_3 composites.[24] The cylindrical pellets of 15-mm diameter and 5-mm thickness were made using a graphite die under a uniaxial pressure of 75 MPa. For the comparison, pure Fe was also milled for 20 hours and consolidated at 973 K and 1073 K (700 °C and 800 °C) in SPS using similar conditions adopted for the consolidation of nanocomposite powders. In order to ensure that the SPS samples are free from graphite or thin layer of carbon contaminant (possibly formed during SPS process), samples of minimum of 2-mm thickness were removed from sintered pellet by belt grinding.

Microstructural analysis was carried out for bulk consolidated samples using Philips CM20 transmission electron microscope (TEM) operating at 200 kV. For the TEM analysis, the samples were prepared by Ar-ion milling preceded by dimpling. After ion milling process, plasma cleaning for 15 minutes was carried out to remove all organic elements from the surface by means of argon and hydrogen gas purging. Density of bulk samples was measured by Archimedes method and average of three measurements was reported. The hardness of the compacts was measured using microhardness tester under a load of 300 g for 15 seconds. Approximately, 20 readings were taken from three different samples, and the average has been reported as the Vickers microhardness value. Yield strength values were obtained from microhardness values by using the conversion formula, HV × 3 MPa. Compression test was carried out on cylindrical sample with 2.5-mm diameter and 3-mm thickness at the strain rate of 10^{-4} s^{-1}.

III. RESULTS

A. *Phase Formation During Milling of Fe_2O_3-Al-Fe*

High-energy ball milling was carried out for Fe_2O_3-2.6 wt pct Al-89.6 wt pct Fe powder mixture in order to synthesize Fe-10 vol pct Al_2O_3 nanocomposite powder. The chemical reaction involved here can be expressed as

$$Fe_2O_3 + Al + Fe \rightarrow Fe + Al_2O_3 \qquad [1]$$

Figure 1 shows the XRD patterns of Fe_2O_3-Al-Fe powder mixture corresponding to Fe-10 vol pct Al_2O_3 as a function of milling time. During reactive milling, the observations made after 5 hours milling are the broadening of the Fe peaks and the decrease in the Fe_2O_3 peak intensity. The decrease in the Fe_2O_3 peak intensity which is almost reduced to zero after 5 hours of milling and the disappearance of Al peak indicate the progress of Fe_2O_3 reduction. The disappearance of Al and Fe_2O_3 peaks after 5 hours of milling cannot be considered as the evidence for the complete reduction of Fe_2O_3. Due to their smaller quantity and nanocrystalline nature, the XRD analysis alone will not be able to confirm the complete reduction. The reduction of Fe_2O_3 can occur during further milling and consolidation. The crystallite size and the lattice strain of Fe with respect to milling time are shown in Figure 2. After 5 hours of milling, the crystallite size and lattice strain of Fe are measured to be 27 nm and 0.59 pct, respectively, and at the end of 20 hours of milling, the crystallite size and lattice strain of Fe are 11 nm and 1.27 pct, respectively. For comparison, pure Fe was also milled for 20 hours. The measured crystallite size and lattice strain of pure Fe after 20 hours of milling are 21 nm and 0.72 pct, respectively. The observation of more reduction in crystallite size and large increase in lattice strain in the Fe_2O_3-Al-Fe powder mixture compared to pure Fe is due to the presence of ceramic particles such as Fe_2O_3 and Al_2O_3.[33]

B. *Phase Formation During Consolidation*

The 20-h-milled Fe_2O_3-Al-Fe powder mixture and 20-hmilled pure Fe was consolidated at 973 K and

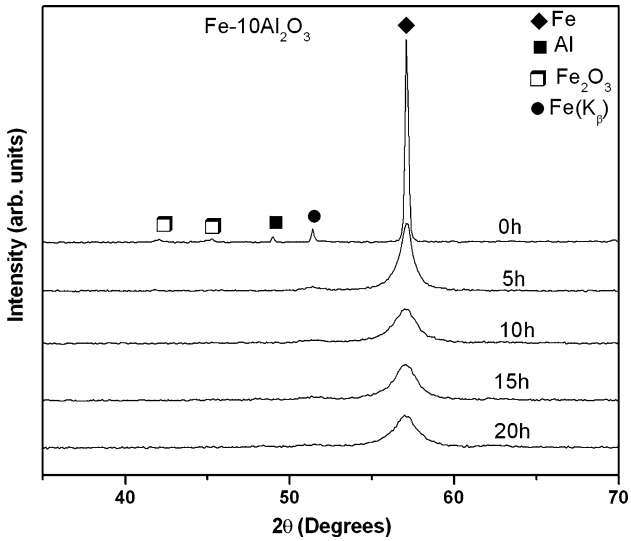

Fig. 1—XRD pattern of Fe_2O_3-Al-Fe powder mixture corresponding to Fe-10 vol pct Al_2O_3 as a function of milling time.

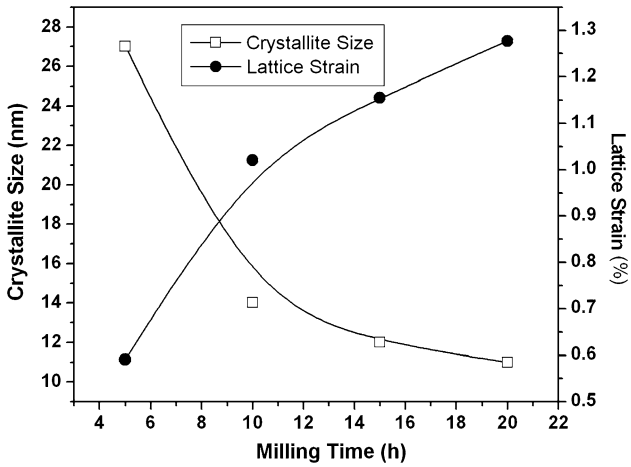

Fig. 2—Crystallite size and lattice strain of Fe in Fe_2O_3-Al-Fe powder mixture corresponding to Fe-10 vol pct Al_2O_3 with respect to milling time.

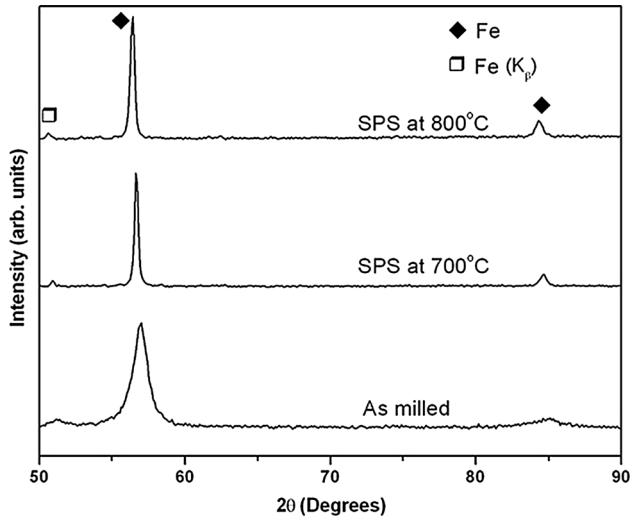

Fig. 3—XRD patterns of pure Fe consolidated at 973 K and 1073 K (700 °C and 800 °C).

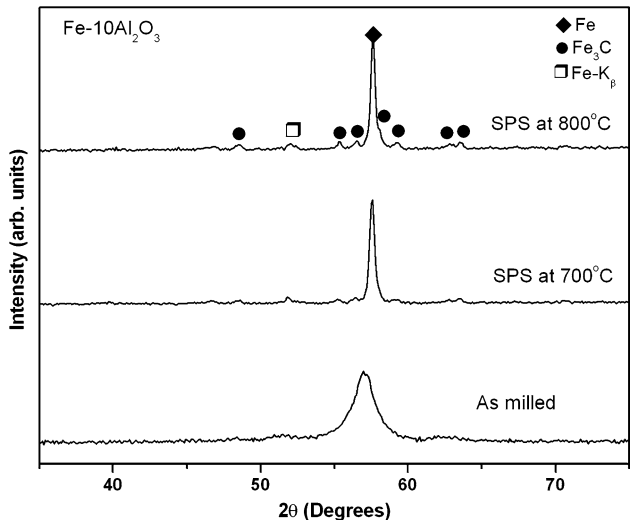

Fig. 4—XRD patterns of Fe-10 vol pct Al_2O_3 consolidated at 973 K and 1073 K (700 °C and 800 °C).

1073 K (700 °C and 800 °C) using SPS. The XRD patterns of the as-milled and sintered Fe consist only the Fe peaks in Figure 3. After the consolidation, coarsening of Fe phase grain is observed by the increase in peak intensity with reduced peak width. In the case of Fe-10 vol pct Al_2O_3, the XRD analysis after the consolidation shows the presence of Fe_3C particles along with reduction in Fe peak (Figure 4). The presence of these Fe_3C particles indicates that the Fe has reacted with process-controlling agent (Toluene). Moreover, the absence of these Fe_3C particles in Fe pellet can be explained on the basis of more reactive nature of nascent Fe which appears due to Fe_2O_3 reduction during reactive milling.

The TEM images of the Fe samples sintered at 973 K and 1073 K (700 °C and 800 °C) are shown in Figures 5 and 6, respectively. The bright-field images in Figures 5(a) and 6(a) show that the grain sizes of Fe are in submicron level after consolidation. The SAD patterns shown in Figures 5(b) and 6(b) consist of diffraction spots as well as continuous diffraction rings. Indexing of SAD pattern reveals the presence of fine Fe_3O_4 particle along with Fe phase.

The dark-field image of Fe phase is obtained from the diffraction spot from Fe (110) plane (Figure 5(c)). The average grain size of the Fe sintered at 973 K (700 °C) is 252 ± 36 nm, and the corresponding grain-size distribution plot is presented in Figure 5(d). After the sintering at 1073 K (800 °C), the average grain size of Fe is increased to 313 ± 172 nm (Figure 6(a)) and the corresponding grain-size distribution plot for Fe consolidated at 1073 K (800 °C) is shown in Figure 6(d). The dark-field image of Fe_3O_4 phase presented in Figure 6(c) shows that the size of Fe_3O_4 particles is ranging from 30 to 40 nm in Fe sample consolidated at 1073 K (800 °C). Based on several dark-field images obtained from different diffraction planes, the volume percentage of Fe_3O_4 is measured approximately as 1 pct.

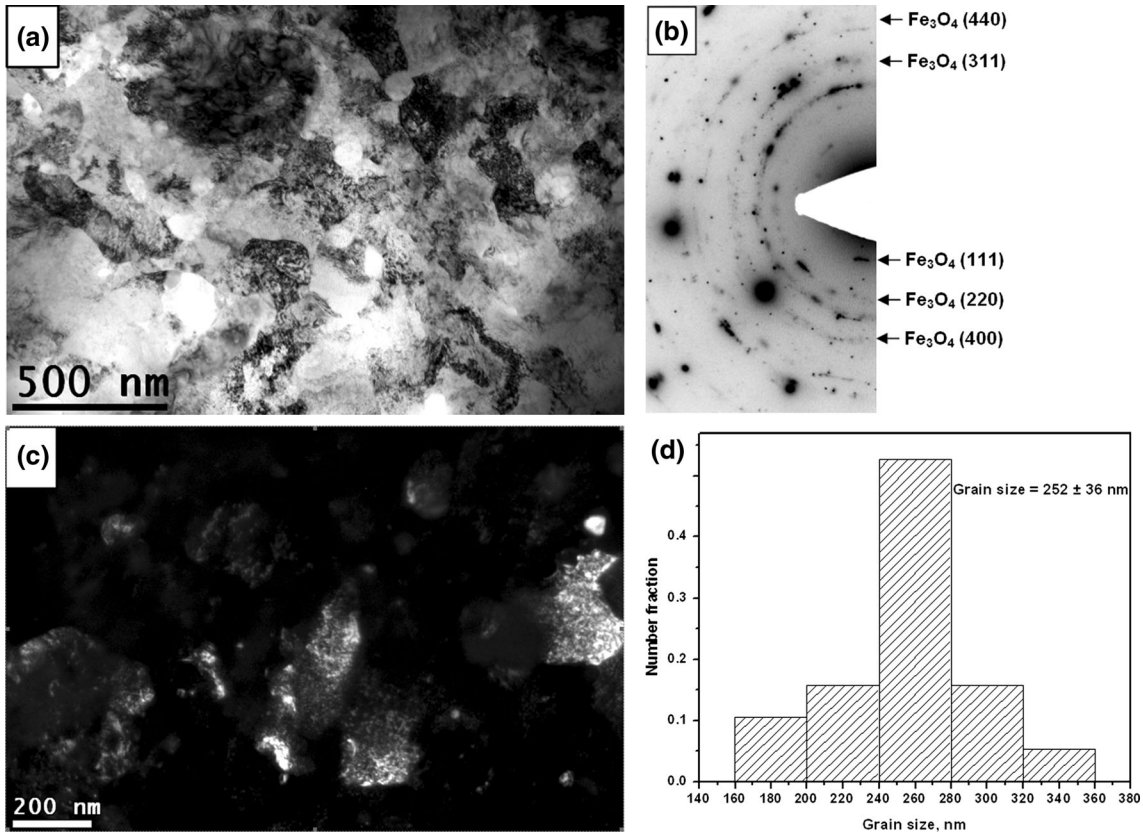

Fig. 5—TEM micrographs of Fe SPS consolidated at 973 K (700 °C), (*a*) bright-field image, (*b*) SAD pattern, (*c*) dark-field image of Fe and (*d*) grain-size distribution of Fe.

The results of TEM studies on the bulk Fe-10 vol pct Al_2O_3 sample consolidated at 973 K (700 °C) are shown in Figure 7. The bright-field image reveals the presence of nanocrystalline and submicron grains (Figure 7(a)). The SAD pattern presented in Figure 7(b) consists of spotty as well as continuous diffraction rings. Indexing of the SAD reveals the presence of Fe_3O_4, Fe_3C, and α-Al_2O_3 along with the Fe phase. The dark-field image of Fe presented in Figure 7(c) shows the wide range of grain sizes of Fe. The grain-size distribution plot for Fe phase is shown in Figure 7(d), and the average grain size is measured to be 75 ± 36 nm.

The results of TEM studies on the bulk Fe-10 vol pct Al_2O_3 sample consolidated at 1073 K (800 °C) are shown in Figure 8. The bright-field image reveals the presence of nanocrystalline-, submicron-, and micro-n-level grains (Figure 8(a)). The grains are coarser, and the grain-size range is wider compared to the sample sintered at 973 K (700 °C). Indexing of the SAD pattern reveals the presence of Fe_3O_4, Fe_3C, and α-Al_2O_3 along with the Fe phase (Figure 8(b)). The dark-field images obtained from α-Al_2O_3 (104) plane suggest uniform distribution of α-Al_2O_3 particle in Fe matrix (Figure 8(c)). The average particle size of α-Al_2O_3 measured from dark-field image in Figure 8(d) reveals that it ranges approximately from 10 to 12 nm. The dark-field images in Figure 8(e) shows the presence of Fe_3O_4 particles of size ranging from 30 to 40-nm. The volume percentage of Fe_3O_4 measured from several dark-field images taken is 5 pct. The grain-size distribution plot for Fe phase shown in Figure 8(f) clearly indicates the bimodal grain-size distribution with an average grain size of 382 ± 285 nm. When we compare the XRD and TEM results of Fe-10 vol pct Al_2O_3 nanocomposites, the α-Al_2O_3 and Fe_3O_4 peaks are absent in XRD results, whereas the SAD pattern reveals their presence. This is due to the finer size as well as the smaller quantity of these phases. The continuous ring pattern observed in TEM-SAD patterns for α-Al_2O_3 and Fe_3O_4 particles supports their finer size. Moreover, the low atomic scattering factor of Al_2O_3 phase also can contribute their absence in XRD pattern. The presence of Fe_3C phase is revealed in both XRD and TEM results. The SAD pattern of Fe_3C is overlapping with other phases like Al_2O_3, Fe_3O_4, and Fe. When the overlapping pattern of other phases is excluded, the Fe_3C phase shows spot pattern. This spot pattern indicates the coarse nature of Fe_3C compared with other secondary-phase particles, and it is believed to be as a reason for the observation of Fe_3C phase in XRD analysis.

C. *Mechanical Properties of Fe and Fe-Al_2O_3 Nanocomposites*

The density, grain size, and the hardness values of the consolidated Fe and Fe-10vol pct Al_2O_3 composites are listed in Table I. The theoretical density was calculated

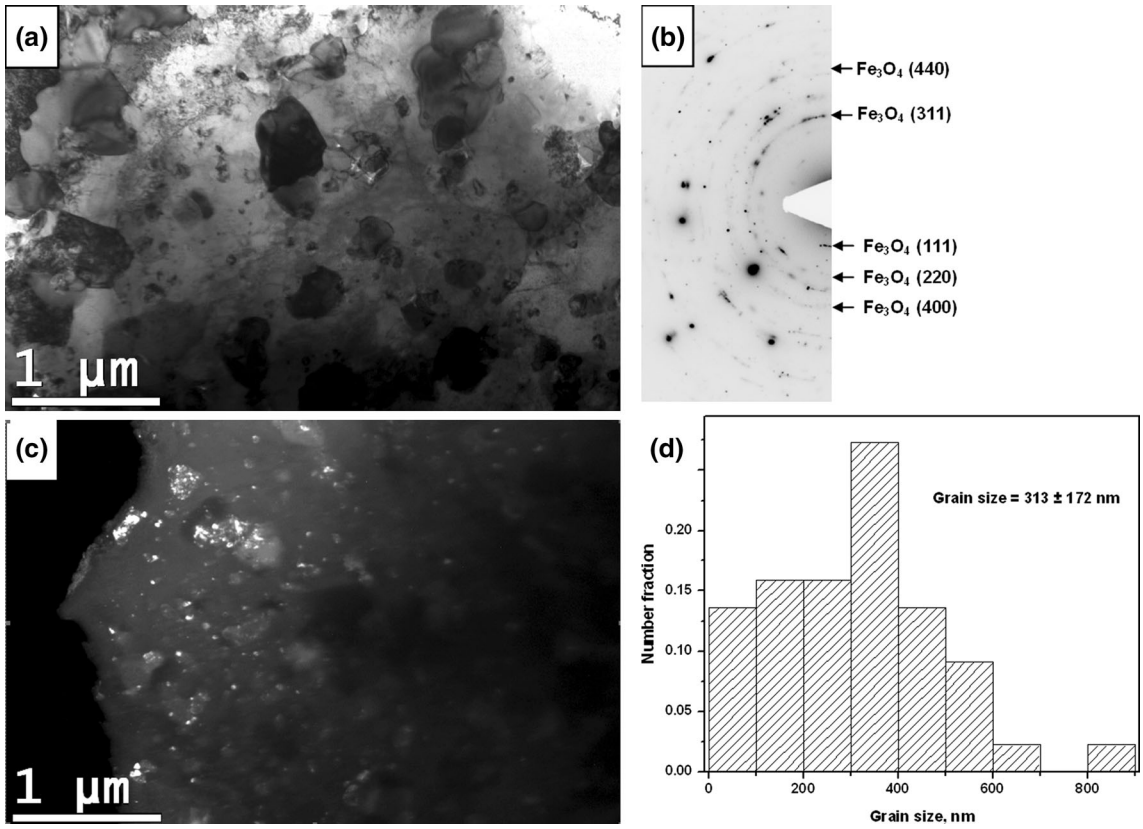

Fig. 6—TEM micrographs of Fe SPS at 1073 K (800 °C) (*a*) bright-field image, (*b*) SAD pattern, (*c*) dark-field image of Fe_3O_4, and (*d*) grain-size distribution of Fe.

by taking into account of appropriate volume percentage of α-Al_2O_3, Fe_3O_4, and Fe_3C particles measured based on TEM analysis. The density values of Fe and Fe-10 vol pct Al_2O_3 after spark plasma consolidation at 1073 K (800 °C) are measured to be 97 and 96 pct of theoretical density, respectively. The hardness values of the nanocomposites are ~2 times higher than those of Fe. A decrease in the hardness is observed as the consolidation temperature is increased from 973 K to 1073 K (700 °C to 800 °C) due to the grain coarsening. Despite the lower density observed, the composite sintered at 973 K (700 °C), displays higher hardness compared to the one sintered at 1073 K (800 °C) due to the presence of nanocrystalline grain size.

The results of compression test conducted on consolidated Fe and Fe-10 vol pct Al_2O_3 are presented in Figure 9. Fe-10 vol pct Al_2O_3 composite sintered at 1073 K (800 °C) has exhibited higher yield strength of 2100 MPa, which is nearly twice that of pure Fe sintered at 973 K and 1073 K (700 °C and 800 °C). However, the reduction in the plastic strain was more in nanocomposite due to large fraction of secondary-phase particles which include α-Al_2O_3, Fe_3O_4, and Fe_3C particles. In the case of Fe-10 vol pct Al_2O_3 nanocomposite sintered at 973 K (700 °C), the yield strength deduced from the hardness is 449 MPa (2349 MPa) that is greater than the yield strength obtained from the compression test (1900 MPa). The possible reason for this larger difference is that the composite sintered at 1073 K (800 °C) got fractured in a brittle manner before yielding because of poor density.

IV. DISCUSSION

A. *Microstructure of Consolidated Fe-Al_2O_3 Nanocomposites*

The XRD and TEM analyses of consolidated samples have shown the presence of additional phases such as Fe_3O_4 and Fe_3C along with the intended Fe and Al_2O_3 phases. Since thermit reaction is being carried out in the reducing atmosphere, *i.e.*, reduction of Fe_2O_3 by Al during ball milling in the presence toluene medium, the formation of Fe_3O_4 is not expected during milling. Cracking of toluene medium can occur during milling result in the formation of nascent C and O atoms. The extended solid solubility which is one of the important features of MA process[2] results in the formation of interstitial solid solutions of Fe with C and O. During the SPS process, the supersaturated C and O precipitate out from the Fe lattice, which can form Fe_3O_4 and Fe_3C phases. This could be the possible reason for the observation of Fe_3O_4 and Fe_3C phases in the spark plasma-sintered Fe-10 vol pct Al_2O_3 nanocomposites. Further to ensure the source of carbon, the as-milled loose powders were heat treated at 1073 K (800 °C) for 5 minutes (to simulate SPS process parameters). XRD analysis of the heat-treated powder reveals the presence

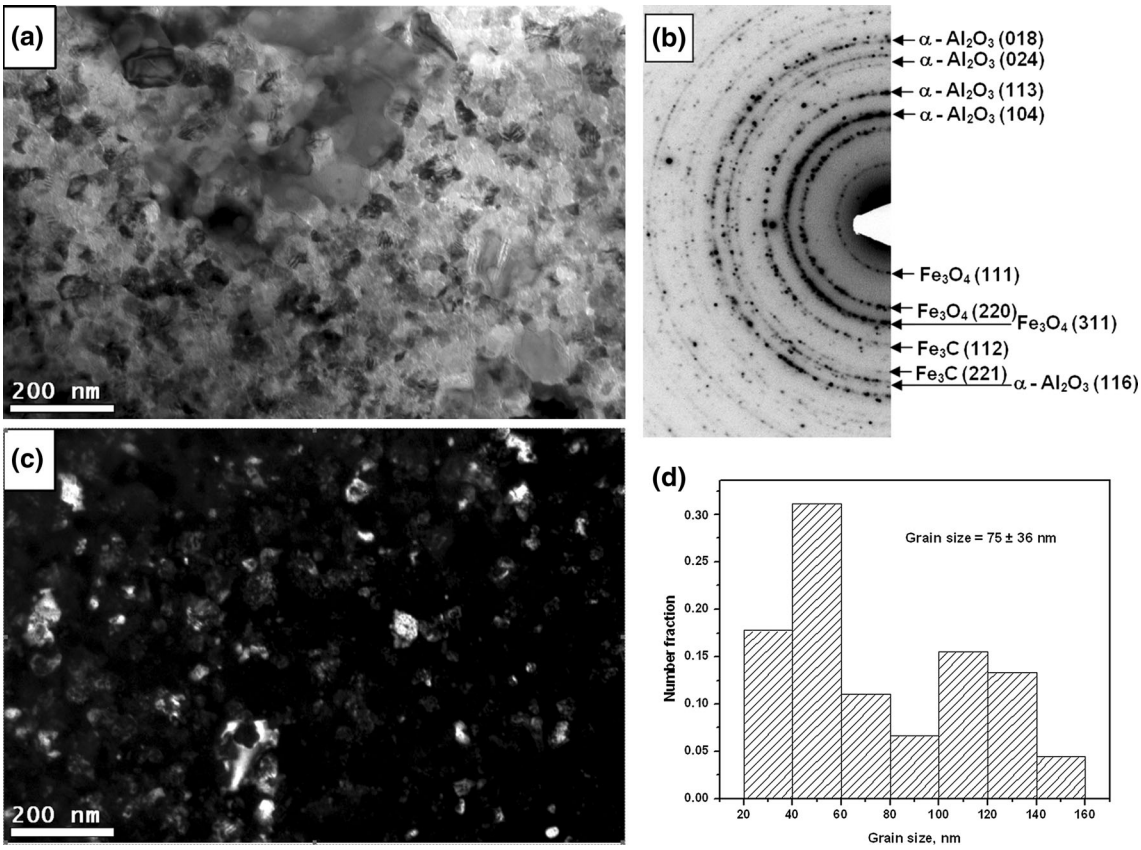

Fig.7—TEM micrographs of Fe-10 vol pct Al_2O_3 consolidated at 973 K (700 °C) (*a*) bright-field image, (*b*) SAD pattern, (*c*) dark-field image of Fe, and (*d*) grain-size distribution of Fe.

Table I. Density, Grain Size, and Hardness Values of Consolidated Fe and Fe-10 vol pct Al_2O_3 Nanocomposites

Composition	SPS Temperature [K (°C)]	Theoretical Density (g/cc)	Measure Density (g/cc)	Density (pct)	Grain Size (nm)	Hardness $HV_{0.3}$
Fe	973 (700)	7.843	7.607	97	252 ± 36	443
	1073 (800)	7.843	7.604	97	313 ± 172	425
Fe-10 vol pct Al_2O_3	973 (700)	7.343	6.755	92	75 ± 36	783
	1073 (800)	7.343	7.041	96	382 ± 295*	714

* Heterogeneous grain structure.

of Fe_3C phase (Figure 10) which confirms that the milling medium toluene is the major carbon source for the formation of Fe_3C phase.

The TEM analysis of Fe-10 vol pct Al_2O_3 nanocomposite sintered at 973 K and 1073 K (700 °C and 800 °C) reveals the bimodal-grained structure of Fe phase and also the presence of fine secondary phase particles (Figures 7 and 8). Fe-10 vol pct Al_2O_3 sintered at 973 K (700 °C) consists of nanometer- and submicron-sized grains. The grains are coarsened, and the bimodal distribution range widens as the sintering temperature is increased to 1073 K (800 °C). Similarly, Srinivasarao *et al.*[27] and Oh-ishi *et al.*[28] have reported bimodal grains in bulk Fe and Fe-0.8C alloys produced by MA and SPS. Moreover, Ji *et al.*[34] have reported bimodal-grained structure in dispersion-strengthened FeAl alloy produced by MA and SPS. Ji *et al.*[34] have stated that the heterogeneous grain structure mainly originates from the high temperature differences generated in the sample during consolidation which is an intrinsic characteristic of the SPS process. Interestingly, observation of significant amount of particles in the microstructure is another common feature noted in the present study and above-cited examples. However, Fe samples sintered at 973 K and 1073 K (700 °C and 800 °C) in the present work have not shown the bimodal-grained structure although the microstructure has small amount (~1 pct) of Fe_3O_4 particles (Figures 5 and 6). Moreover, the authors' earlier studies on Ni-Al_2O_3,[16] and NiAl-Al_2O_3 nanocomposites[17,18] produced by MA and SPS did not show bimodal-grained structure. Hence, the report that the heterogeneous-grained

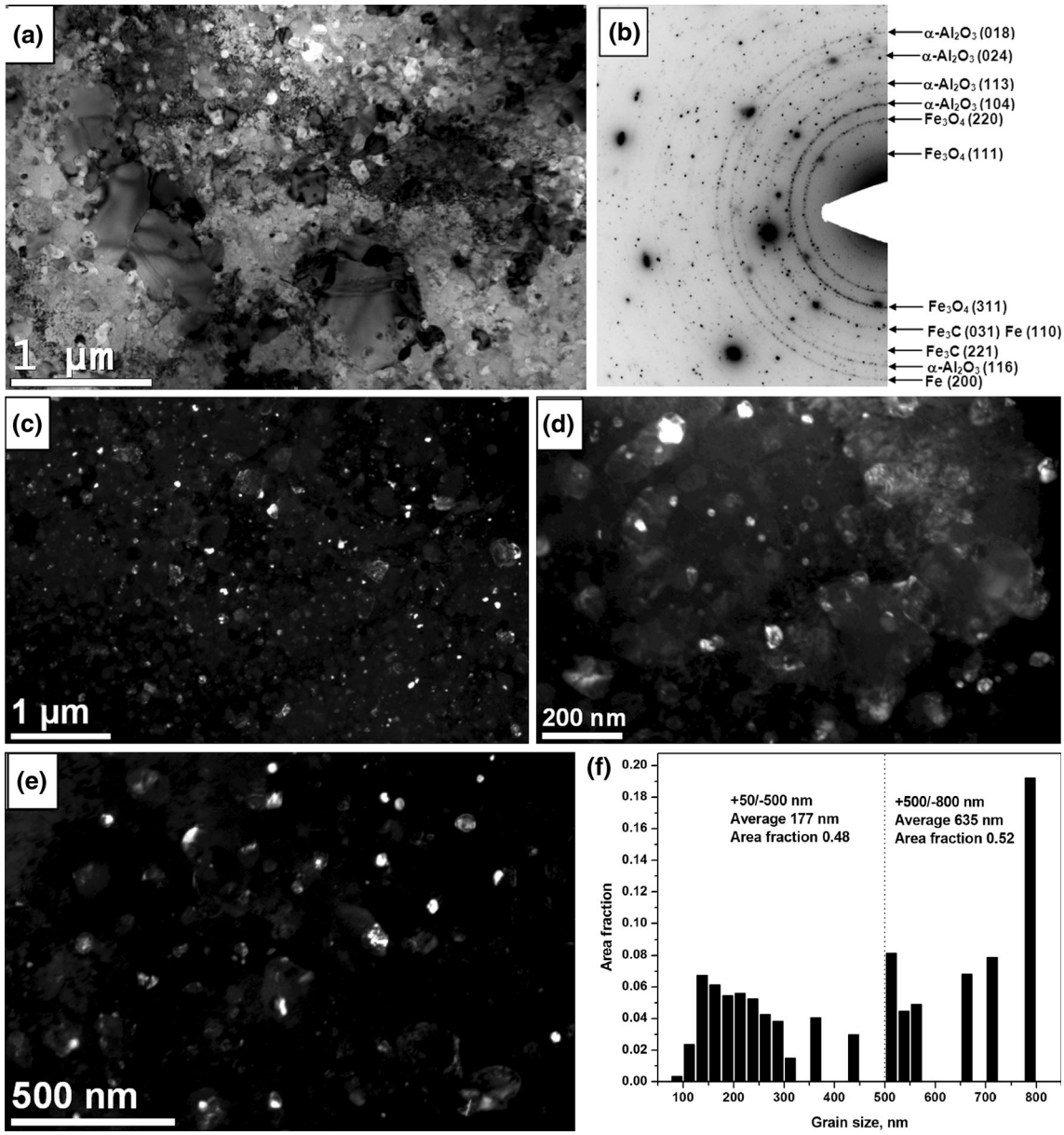

Fig. 8—TEM micrographs of Fe-10 vol pct Al_2O_3 consolidated at 1073 K (800 °C). (*a*) bright-field image, (*b*) SAD pattern, (*c*) and (*d*) dark-field images of α-Al_2O_3, (*e*) dark-field images of Fe_3C and Fe_3O_4, and (*f*) grain-size distribution of Fe.

structure is an intrinsic characteristic of the SPS process is ambiguous, and hence, further studies for understanding better about the development of heterogeneous-grained structure during SPS are needed.

B. *Strengthening Mechanisms in Fe-Al_2O_3 Nanocomposite*

Figure 11 summarizes the previously published mechanical properties obtained from compression test for nanocrystalline and ultrafine-grained Fe-based materials,[27,28,34–40] in which yield strength is plotted as a function of plastic strain. Note that the previously reported data follow a tradeoff relationship between yield strength and plastic strain. Bulk nanocrystalline Fe materials produced by cold compaction followed by hot pressing have very high yield strength about 2300 MPa but a very low plastic strain of less than 5 pct.[35] The reason for the low plastic strain is attributed to the inability of dislocation activities in the nanocrystalline microstructure which results in shear banding as the dominant deformation mechanism.[35]

Nearly fully dense compacts produced by hot isostatic pressing at about 873 K (600 °C) after mechanical milling of Fe alloys have shown little plastic strains in compression even though the strength level ranged from 1200 to 1500 MPa.[36,37] Such a low plastic strain has resulted from the occurrence of localized deformation[35] and the existence of residual porosity.[37] Ultrafine-grained materials by severe plastic deformation such as ECAP have a high plastic strain ranging from 20 to 30

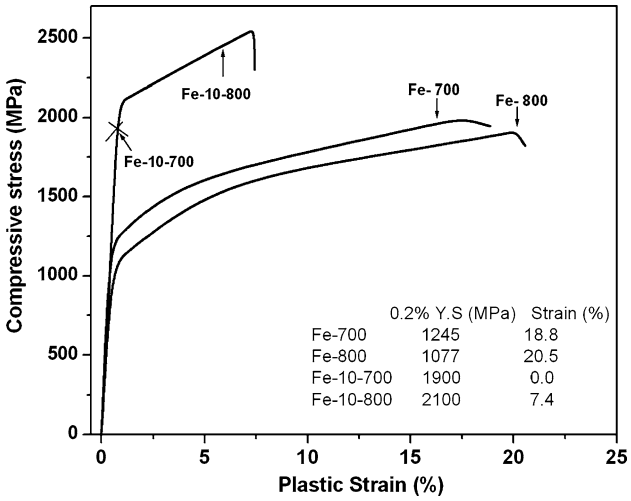

Fig. 9—Compressive stress–strain plots for Fe and Fe-10 vol pct Al_2O_3 nanocomposites.

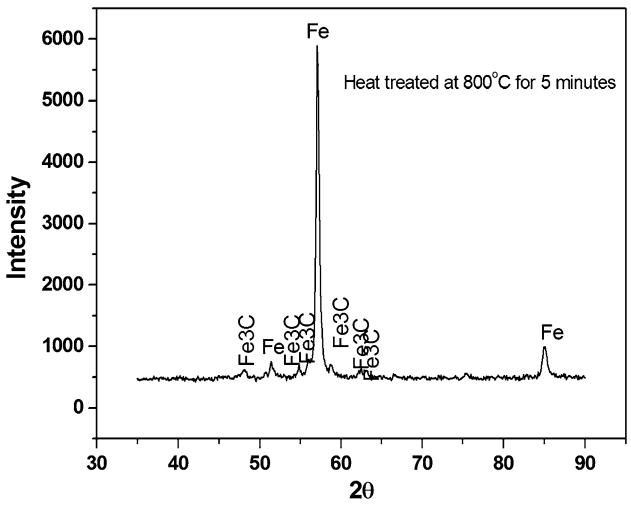

Fig. 10—XRD pattern of Fe_2O_3-Al-Fe powder mixture corresponding to Fe-10 vol pct Al_2O_3 heat treated at 1073 K (800 °C) for 5 min.

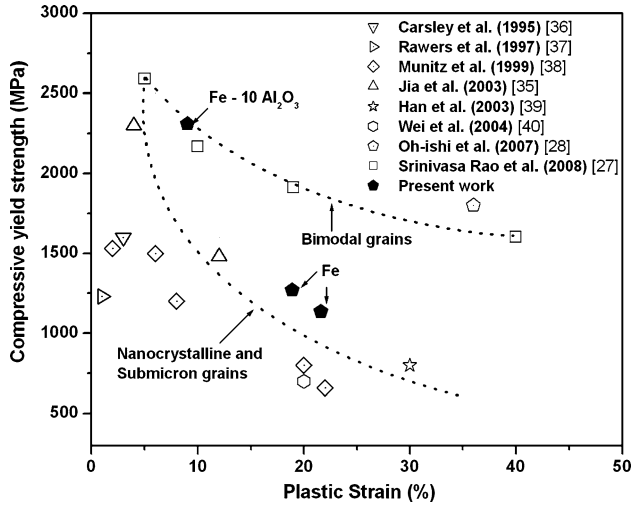

Fig. 11—Plot showing comparison of compressive yield strength values of Fe and Fe-10Al_2O_3 nanocomposite with the literature data on Fe.

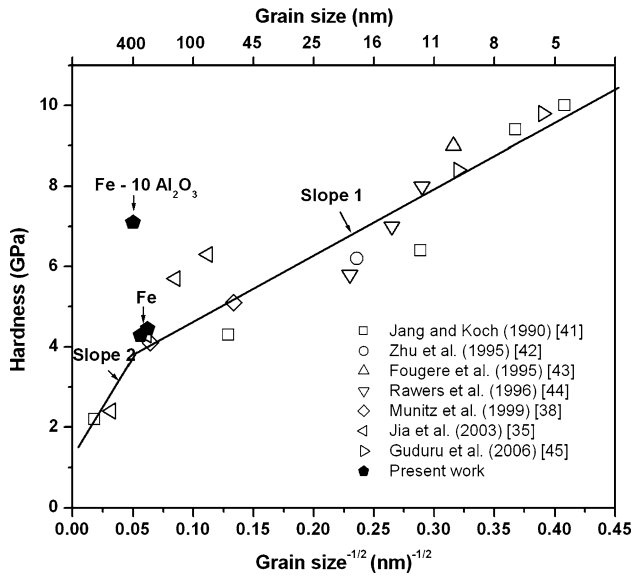

Fig. 12—Hall-Petch plot for Fe using hardness *vs* (grain size)$^{-½}$.

pct, but relatively a low yield strength of ~800 MPa.[38–40] On the other hand, Srinivasarao *et al.*[27] and Oh-ishi *et al.*[28] have shown that the bulk Fe sample produced by SPS has exhibited high yield strength and plastic deformation. When the yield strength and plastic strain obtained in the present work are compared with the literature values, Fe-10 vol pct Al_2O_3 nanocomposite rest on the bimodal grains plot, whereas Fe sintered at 973 K and 1073 K (700 °C and 800 °C) rest on the nanocrystalline and submicron grains plot. Moreover, the microstructural results by TEM analysis support the aforementioned observation. In the bimodal grain-size range, the results obtained in the present work for Fe-10 vol pct Al_2O_3 nanocomposite are comparable with the Srinivasarao *et al.*[27] and Oh-ishi *et al.*[28] works on Fe and Fe-0.8C, respectively. Since the Fe-10 vol pct Al_2O_3 nanocomposite contains considerable amount of reinforcement particles, the yield strength value obtained in the present work is expected to be higher than those of Fe and Fe-0.8C. To understand the possible reason for this observation, the strengthening mechanism involved in the Fe-10 vol pct Al_2O_3 nanocomposite is analyzed.

Microstructural analysis of Fe-10 vol pct Al_2O_3 nanocomposite sintered at 1073 K (800 °C) has revealed the submicron grains with a certain portion of recrystallized coarse grains together with the uniformly dispersed nanosized α-Al_2O_3 and Fe_3O_4 particles. These microstructural features are thus expected to contribute significantly to the material yield strength. In such a condition, yield strength of composite can be represented by

$$\sigma_{0.2} = \sigma_m + \frac{k}{\sqrt{D}} + \sigma_{\alpha-Al_2O_3} + \sigma_{Fe_3O_4} + \sigma_{Fe_3C} \qquad [2]$$

The strengthening contribution from matrix and grain size can be deduced from Hall-Petch plot. To this end, a Hall-Petch plot has been developed using the hardness and grain-size values for Fe available in the literature[41–45] (Figure 12). The Hall-Petch plot for Fe presented in the Figure 12 consists of two lines with different slopes. One line is extended up to 400-nm grain-size regime (Slope 1), and the other line is extended above 400 nm (Slope 2). The hardness values of Fe and Fe-Al_2O_3 nanocomposites in the present work lie in the line 1 and line 2, respectively. According to Figure 12, the strengthening contribution from the matrix and grain size in Fe-10 vol pct Al_2O_3 nanocomposite are calculated to be 3.7 GPa and the remaining 3.4 GPa strengthening is derived from the presence of α-Al_2O_3, Fe_3C, and Fe_3O_4 particles.

Size of Fe_3C phase could not be measured accurately from dark-field image because of its overlapping SAD patterns with other phases. Moreover, spotty SAD patterns suggest the coarse nature of Fe_3C, and hence it is not expected to provide sufficiently large contribution in strengthening. Based on the aforementioned reasons, strengthening contribution derived from Fe_3C phase is assumed to be negligible in the strengthening calculation. TEM observation of Fe-10 vol pct Al_2O_3 nanocomposite shows that approximately 10 vol pct of α-Al_2O_3 particles of sizes ranging from 15 to 20-nm and 5 vol pct of Fe_3O_4 particles of sizes ranging from 30 to 40-nm are distributed uniformly in the Fe matrix. Since the size of uniformly distributed α-Al_2O_3 and Fe_3O_4 particles are much smaller than the Fe matrix (420 nm), Orowan-type strengthening expected to occur. Hence, the strengthening contribution from these particles is calculated using following equation.[16]

$$\sigma_{\text{uni}} = \Delta\sigma_{\text{Oro}} = \frac{2mGb\ln\left\{\frac{\phi}{2b}\right\}}{[(1.18)4\pi(\lambda-\phi)]} \quad [3]$$

where $\Delta\sigma_{\text{Oro}}$ is the Orowan stress or the stress needed to pass a dislocation through an array of impeding particles, m is the Taylor factor taken as 2.5 for Fe, G is the shear modulus, b is the Burgers vector, ϕ is the particle size, and λ is the planar interparticle separation: $\lambda = \phi/\sqrt{f_v}$, where f_v is the volume fraction of particle phase.

The parameters required for the calculation of yield strength of Fe-10 vol pct Al_2O_3 nanocomposites using Orowan strengthening model are given in Tables II and III. Figure 13 shows the theoretically calculated strengthening contribution of α-Al_2O_3 and Fe_3O_4 particles with different sizes and volume fractions based on the Orowan strengthening model. The theoretically calculated yield strength of Fe-10 vol pct Al_2O_3 nanocomposite closely matches with the experimental results (Table IV).

The compressive yield strength values of Fe reported by Srinivasarao *et al.*[27] have been converted to hardness and fitted using Hall-Petch approach in order to compare their results with the literature data (Figure 14). Higher hardness values approximately ranging from 3.2 to 3.5 GPa have been observed compared to the literature data for the similar grain sizes. It has been stated by those authors that the higher hardness is mainly attributed to the presence of fine Cr_2O_3 and Fe_3O_4 particles of 4-10-nm size. In the present study, similar amount of strengthening has been derived from α-Al_2O_3 and Fe_3O_4 particles in Fe-10 vol pct Al_2O_3 nanocomposite although the amounts and sizes of the particles are not the same. The observed bimodal-grained structure and the similar strengthening contribution from the secondary-phase particles support the decline of the hardness values of Fe-10 vol pct Al_2O_3 nanocomposites in bimodal grains plot presented in Figure 14.

Table II. Parameters Used in Theoretical Calculation of Yield Strength in Fe-10 Volume Percent Al_2O_3 Nancomposites

Parameter, unit	Value	Reference
m	2.5	41
G, GPa	75	41
b, nm	0.29	41

Table III. Experimentally Obtained Parameters Used in Theoretical Calculation of Yield Strength in Fe-10 Volume Percent Al_2O_3 Nancomposites

		α-Al_2O_3		Fe_3O_4	
System	Sintering Temperature [K(°C)]	Size (nm)	Volume Fraction	Size (nm)	Volume Fraction
Fe-10 vol pct Al_2O_3	1073 (800)	15 to 20	0.1	30 to 40	0.05

Table IV. Comparison of Theoretically Calculated Yield Strength of Fe-10 Volume Percent Al_2O_3 with Experimental Value

System	Theoretical (MPa)		Experimental (MPa)
Fe-10 vol pct Al_2O_3	matrix + grain size	1240	
	α-Al_2O_3	630 to 780	compression = 2100
	Fe_3O_4	230 to 290	hardness = 2170
	total	2100 to 2310	

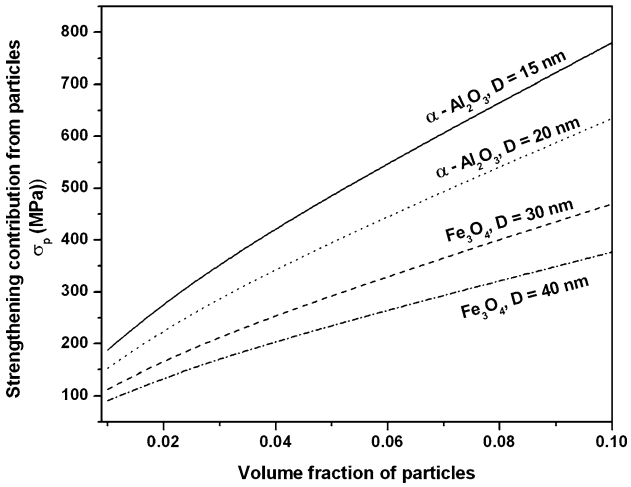

Fig. 13—Theoretically calculated strengthening contribution of particles using Orowan model.

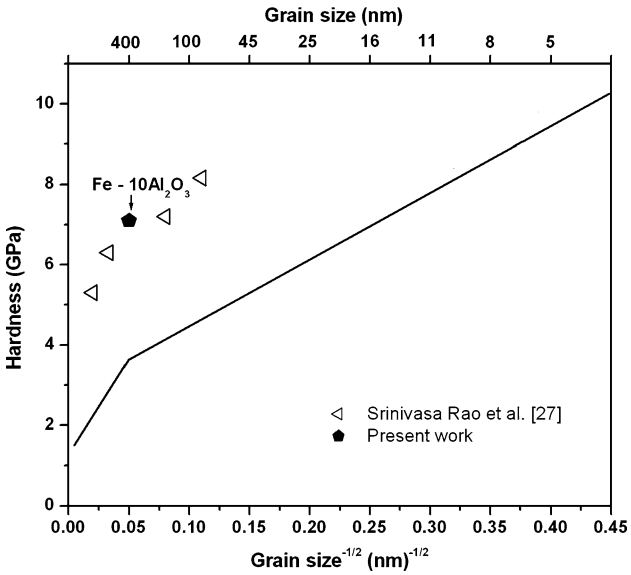

Fig. 14—Hall-Petch plot for Fe and Fe-10 vol pct Al_2O_3 nanocomposite.

To have better understanding about the influences of particles' amount and the size on the yield strength and plasticity, compressive test results of synthesized nanocomposite from the present work have been compared to the results of Srinivasarao *et al.*[27] work by making a plot between compressive yield strength and plasticity *vs* volume fraction of coarse grains (Figure 15). For the similar fraction of coarser grain size, we have obtained 200 MPa higher yield strength for Fe-10 vol pct Al_2O_3 nanocomposite. However, the plastic strain value of Fe-10 vol pct Al_2O_3 composite is 12 pct lower for the similar fraction of coarser grain size. The possible reason for higher yield strength and lower plastic strain of Fe-10 vol pct Al_2O_3 nanocomposite is attributed to the presence of greater amount of coarser particles.

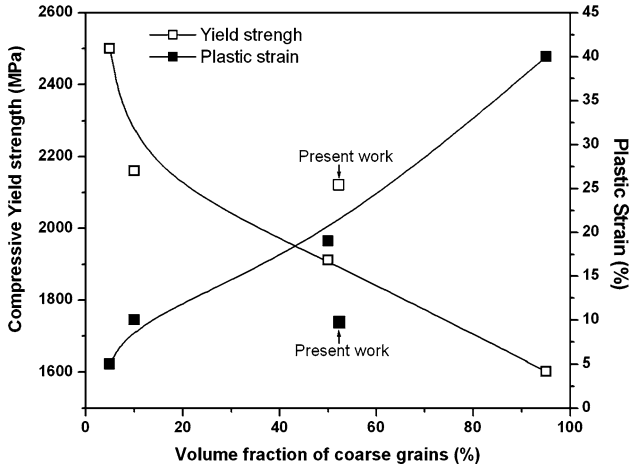

Fig. 15—Plot of compressive yield strength and plastic strain *vs* volume fraction of coarse grains.

V. CONCLUSIONS

Bulk Fe-10 vol pct Al_2O_3 *in situ* nanocomposite has been developed successfully by subjecting Fe_2O_3-Al-Fe powder mixture to high-energy ball milling and consolidating the as-milled powder using SPS. The bulk Fe-10 vol pct Al_2O_3 nanocomposite consist of heterogeneous microstructure covering nanocrystalline- and submicron-sized grains. Fe-10 vol pct Al_2O_3 nanocomposite sintered at 1073 K (800 °C) has higher compressive yield strength of 2100 MPa with 7.4 pct plastic strain. The presence of Al_2O_3 and Fe_3O_4 particles of nanometer size is attributed for the improved compressive yield strength in the synthesized Fe-10 vol pct Al_2O_3 nanocomposites in comparison with Fe.

REFERENCES

1. R. Casati and M. Vedani: *Metals*, 2014, vol. 4, pp. 65–83.
2. B.S. Murty and S. Ranganathan: *Int. Mater. Rev.*, 1998, vol. 43, pp. 101–41.
3. P. Matteazzi and G. Le Caer: *J. Am. Ceram. Soc.*, 1992, vol. 75, pp. 2749–53.
4. G.B. Schaffer and P.G. McCormick: *Metall. Mater. Trans. A*, 1990, vol. 21A, pp. 2789–94.
5. X. Shengqi, Q. Xiaoyan, M. Mingliang, Z. Jingen, Z. Xiulin, and W. Xiaotian: *J. Alloys Compd.*, 1998, vol. 268, pp. 211–14.
6. D.Y. Ying and D.L. Zhang: *Mater. Sci. Eng. A*, 2000, vol. 286, pp. 152–56.
7. D. Oleszak and M. Krasnowski: *Mater. Sci. Forum*, 2001, vols. 360–362, pp. 235–40.
8. D. Oleszak: *J. Mater. Sci.*, 2004, vol. 39, pp. 5169–74.
9. J. Li, F. Li, and K. Hu: *J. Mater. Proc. Tech.*, 2004, vol. 147, pp. 236–40.
10. S.J. Hwang and J.H. Lee: *Mater. Sci. Eng. A*, 2005, vol. 405, pp. 140–46.
11. T. Venugopal, K. Prasad Rao, and B.S. Murty: *Mater. Sci. Eng. A*, 2005, vol. 393, pp. 382–86.
12. B.S.B. Reddy, K. Rajasekhar, M. Venu, J.J.S. Dilip, S. Das, and K. Das: *J. Alloys Compd.*, 2008, vol. 465, pp. 97–105.
13. J.B. Fogagnolo, E.M.J.A. Pallone, D.R. Martin, C.S. Kiminami, C. Bolfarini, and W.J. Botta: *J. Alloys. Compd.*, 2009, vol. 471, pp. 448–52.

14. S.Z. Anvari, F. Karimzadeh, and M.H. Enayati: *J. Alloys Compd.*, 2009, vol. 477, pp. 178–81.
15. V. Udhayabanu, K.R. Ravi, V. Vinod, and B.S. Murty: *Intermetallics*, 2010, vol. 18, pp. 353–58.
16. V. Udhayabanu, K.R. Ravi, K. Murugan, D. Sivaprahasam, and B.S. Murty: *Metall. Mater. Trans. A*, 2011, vol. 42A, pp. 2085–93.
17. V. Udhayabanu, K.R. Ravi, and B.S. Murty: *J. Alloys Compd.*, 2011, vol. 509S, pp. S223–28.
18. V. Udhayabanu, K.R. Ravi, and B.S. Murty: *Mater. Sci. Eng. A*, 2013, vol. 585, pp. 379–86.
19. M.P. Horvath and L. Takacs: *IEEE Trans. Magn.*, 1992, vol. 28, pp. 3186–88.
20. L. Takacs: *Mater. Lett.*, 1992, vol. 13, pp. 119–24.
21. P. Matteazzi, F. Miani, and D. Basset: *Nanostruct. Mater.*, 1993, vol. 2, pp. 355–60.
22. P.M. Botta, R.C. Mercader, E.F. Aglietti, and J.M. Porto: Lopez*Scripta Mater.*, 2003, vol. 48, pp. 1093–98.
23. K. Isonishi, M. Hashii, and K. Ameyama: *JSME Int. J. Series A*, 2006, vol. 49, pp. 229–36.
24. K.R. Ravi, A. Murugesan, V. Udhayabanu, R. Subramanian, and B.S. Murty: *Mater. Sci. Forum*, 2012, vol. 710, pp. 291–96.
25. M. Khodaei, M.H. Enayati, and E.F. Karimzadeh: *J. Mater. Sci.*, 2008, vol. 43, pp. 132–38.
26. R. Orrù, R. Licheri, A.M. Locci, A. Cincotti, and G. Cao: *Mater. Sci. Eng. R.*, 2009, vol. 63, pp. 127–287.
27. B. Srinivasarao, K. Oh-ishi, T. Ohkubo, T. Mukai, and K. Hono: *Scripta Mater.*, 2008, vol. 58, pp. 759–62.
28. K. Oh-ishi, H.W. Zhang, T. Ohkubo, and K. Hono: *Mater. Sci. Eng. A*, 2007, vol. 456, pp. 20–27.
29. Y. Long, T. Wang, H.Y. Zhang, and X.L. Huang: *Mater. Sci. Eng. A*, 2014, vol. 608, pp. 82–89.
30. D. Tingaud, P. Jenei, A. Krawczynska, F. Mompiou, J. Gubicza, and G. Dirras: *Mater. Char.*, 2015, vol. 99, pp. 118–27.
31. Z. Li, Z. Lua, R. Xiea, C. Lua, and C. Liu: *Mater. Sci. Eng. A*, 2016, vol. 660, pp. 52–60.
32. T.H. De Keijser, J.I. Langford, E.J. Mittemeijer, and A.B.P. Vogel: *J. Appl. Crys.*, 1982, vol. 15, pp. 308–14.
33. I. Cvijovic, M. Vilotijevic, and T.J. Milan: *Mater. Char.*, 2006, vol. 57, pp. 94–99.
34. G. Ji, T. Grosdidier, N. Bozzolo, and S. Launois: *Intermetallics*, 2007, vol. 15, pp. 108–18.
35. D. Jia, K.T. Ramesh, and E. Ma: *Acta Mater.*, 2003, vol. 51, pp. 3495–509.
36. J.E. Carsley, W.W. Milligan, S.A. Hackney, and E.C. Aifantis: *Metall. Mater. Trans. A*, 1995, vol. 26A, pp. 2479–81.
37. J. Rawers, R. Krabbe, and N. Duttlinger: *Mater. Sci. Eng. A*, 1997, vol. 230, pp. 139–45.
38. A. Munitz, Z. Livne, J.C. Rawers, J.S. Adams, and R.J. Fields: *Nanostruct. Mater.*, 1999, vol. 11, pp. 159–77.
39. B.Q. Han, E.J. Lavernia, and F.A. Mohamed: *Metall. Mater. Trans. A*, 2003, vol. 34A, pp. 71–83.
40. Q. Wei, L. Kecskes, T. Jiao, K.T. Hartwig, K.T. Ramesh, and E. Ma: *Acta Mater.*, 2004, vol. 52, pp. 1859–69.
41. J.S.C. Jang and C.C. Koch: *Scripta Metall. Mater.*, 1990, vol. 24, pp. 1599–604.
42. M. Zhu and H.J. Fecht: *Nanostruct. Mater.*, 1995, vol. 6, pp. 921–24.
43. G.E. Fougere, J.R. Weertman, and R.W. Siegel: *Nanostruct. Mater.*, 1995, vol. 5, pp. 127–34.
44. J. Rawers, G. Slavens, D. Govier, D. Dogan, and R. Doan: *Metall. Mater. Trans. A*, 1996, vol. 27A, pp. 3126–34.
45. R.K. Guduru, R.O. Scattergood, C.C. Koch, K.L. Murty, S. Guruswamy, and M.K. McCarter: *Scripta Mater.*, 2006, vol. 54, pp. 1879–83.